



# Construction of multi-dimensional core/shell Ni/NiCoP nano-heterojunction for efficient electrocatalytic water splitting

Yan Lin<sup>a,b</sup>, Yuan Pan<sup>b,\*</sup>, Shoujie Liu<sup>c</sup>, Kaian Sun<sup>b</sup>, Yuansheng Cheng<sup>d</sup>, Ming Liu<sup>b</sup>, Zhaojie Wang<sup>a</sup>, Xiyu Li<sup>a</sup>, Jun Zhang<sup>a,b,\*</sup>

<sup>a</sup> School of Materials Science and Engineering, China University of Petroleum (East China), Qingdao, 266580 China

<sup>b</sup> State Key Laboratory of Heavy Oil Processing, China University of Petroleum (East China), Qingdao, 266580, China

<sup>c</sup> College of Chemistry and Materials Science, Anhui Normal University, Wuhu, 241000, China

<sup>d</sup> School of Chemistry and Engineering, Anhui University of Technology, Maanshan, 243002, China

## ARTICLE INFO

### Keywords:

Nanocrystals synthesis

Heterojunction

XANES and EXAFS

Electrocatalyst

Water splitting

## ABSTRACT

Tuning structure, morphology and electronic state of electrocatalysts is essential to achieve highly efficient water splitting. Herein, we report synthesis of snap bean-like multi-dimensional core/shell Ni/NiCoP nano-heterojunctions (NHs) by adopting a solid phase transformation strategy. In the special structure, Ni nanoparticles are enclosed and strung by single phased NiCoP, forming strings of Ni/NiCoP core/shell heterojunctions, which showed improved stability and activity for both hydrogen evolution (HER) and oxygen evolution reactions (OER). X-ray photoelectron spectroscopy and synchrotron-radiation-based X-ray absorption spectroscopy reveal that interactions at the interface of Ni/NiCoP greatly changed electronic structures, which is a key intrinsic factor to underpin the enhanced electrocatalytic performance. Density functional theory calculations demonstrate Ni/NiCoP interface provide more optimal binding strength for H adatom and H<sub>2</sub>O molecule for HER, strong capture of hydroxyl, high valence Ni/Co species for OER. All these peculiarities facilitate the electrocatalytic process: only 1.57 V was needed to reach the current density of 10 mA·cm<sup>-2</sup> for the overall water splitting using Ni/NiCoP NHs as both electrodes. This work demonstrates a facile strategy for synthesis of sophisticated catalytic interface at nano level and endows nano-heterojunction catalysts with enhanced performance for catalytic applications.

## 1. Introduction

Hydrogen is one of the most promising energy candidates with slight ecological impact [1]. Producing hydrogen by water electrolysis is a desired way [2,3]. But both of the two half-reactions (hydrogen and oxygen evolution reaction, HER and OER) are kinetically sluggish and need electrocatalysts to reduce the additional energy expenditure [4,5]. Many studies were focusing on replacing the high cost HER or OER noble metal catalysts (Pt, RuO<sub>2</sub> and IrO<sub>2</sub>) [6,7]. However, most of the reported catalysts performed well only for one half reaction, or effective in one kind of electrolyte condition. Previous studies have suggested that non-noble metal Ni has a moderate hydrogen binding energy similar to that of Pt and might be a promising candidate for catalyzing both HER and OER [8–10]. However, Ni metal is unstable under acid conditions due to dissolution. Alternatively, some transition metal phosphides were found to possess electronic structure similar to [NiFe] hydrogenase, thus are promising catalysts for HER process [6], despite

the introduction of more electronegative nonmetallic P degraded the conductivity. Recent researches revealed bimetallic phosphide nanostructures displayed superior electrocatalytic performance for both HER and OER compared to their single metallic counterparts, owing to the enhanced proton discharge efficiency and synergistic effect [11–15].

To achieve both high activity and stability comparable to those of Pt, rational design and controlled synthesis of hybrid nanostructures with desired interface and structure are essential [16–19]. Herein, we first synthesized multi-dimensional Ni/NiCoP nano-heterojunctions (NHs) by a solid-state phase transformation (SPT) strategy. In the special structure, metallic Ni nanoparticles (NPs) are enclosed and strung by NiCoP, forming strings of Ni/NiCoP core/shell nanostructures. This particular structure takes the most of advantages of Ni metal and bimetallic phosphides nanostructures, but avoids the disadvantages. More significantly, X-ray photoelectron spectroscopy (XPS) and synchrotron-radiation-based X-ray absorption spectroscopy (XAS) studies show that the Ni/NiCoP interface brings unique electronic structure. Additionally,

\* Corresponding authors at: State Key Laboratory of Heavy Oil Processing, China University of Petroleum (East China), Qingdao, 266580, China.

E-mail addresses: [panyuan@upc.edu.cn](mailto:panyuan@upc.edu.cn) (Y. Pan), [zhangj@upc.edu.cn](mailto:zhangj@upc.edu.cn) (J. Zhang).

<https://doi.org/10.1016/j.apcatb.2019.118039>

Received 15 March 2019; Received in revised form 15 June 2019; Accepted 1 August 2019

Available online 06 August 2019

0926-3373/© 2019 Elsevier B.V. All rights reserved.

density functional theory (DFT) calculations demonstrate the formation of Ni/NiCoP interface promotes the rate limiting step in HER process by weakening the strong binding of H adatom and optimizing the adsorption energy of  $\text{H}_2\text{O}$  molecule, and the interface sites also provide strong capture of hydroxyl, high valence Ni/Co species for OER. All of these peculiarities contribute to the positive discovery: a comparable HER activity to commercial Pt/C especially in alkaline, better OER activity than  $\text{IrO}_2$ . And only 1.57 V was needed to drive overall water splitting current density to  $10 \text{ mA} \cdot \text{cm}^{-2}$  using Ni/NiCoP NHs as both electrodes in alkaline.

## 2. Experimental details

### 2.1. Materials

Nickel (II) acetylacetonate ( $\text{Ni}(\text{acac})_2$ , 95%), cobalt (II) acetylacetonate ( $\text{Co}(\text{acac})_2$ , 97%), trioctylphosphine (TOP, 90%) and oleylamine (OAm, 80%~90%) were obtained from Aladdin Chemistry Co. Ltd. 1-octadecene (ODE, tech. 90%) was purchased from Tokyo Chemical Industry (TCI). Hexane ( $\geq 99.5\%$ ), ethanol ( $\geq 99.7\%$ ), potassium hydroxide (KOH,  $\geq 85\%$ ) and sulfuric acid ( $\text{H}_2\text{SO}_4$ , 98%) were all purchased from Sinopharm Chemical Reagent Co. Ltd. All the reagents are used as received.

### 2.2. Synthesis procedures

CoP precursor solution.  $\text{Co}(\text{acac})_2$  (0.256 g), OAm (10 mL) and ODE (5 mL) were placed in a three-neck flask and stirred magnetically about 20 min under a flow of nitrogen (99.999%). The mixture was heated to  $120^\circ\text{C}$  and maintained for 30 min to remove low boiling solvent and dissolved oxygen. Then, 1 mL TOP was quickly injected into the solution by an injector, the mixture was rapidly heated to  $330^\circ\text{C}$  and maintained for 1 h. The black precipitate was separated and washed by adding excess hexane and ethanol (Vhexane: Vethanol = 1:3). Finally the product was dispersed in 5 mL ODE for further use.

Ni/NiCoP NHs.  $\text{Ni}(\text{acac})_2$  (0.256 g) and OAm (10 mL) were added to a three-neck flask, the mixed solution was heated to  $50^\circ\text{C}$ , then 5 mL CoP precursor solution was added, and nitrogen was through to the flask for about 20 min, heated the solution to  $120^\circ\text{C}$  and maintained for 1 h to remove low boiling solvent and dissolved oxygen, and then the solution was heated to  $320^\circ\text{C}$  for 2 h. The samples of 1:0.1, 1:0.3, 1:0.5, 1:0.8 and 1:1.2 can be obtained by changing the dosages of the Ni ( $\text{acac})_2$  to 0.026, 0.077, 0.128, 0.204 and 0.307 g.

NiCoP nanocrystals (NCs). The process for preparing NiCoP nanoparticle is similar with the Ni/NiCoP NHs, except another 1 mL TOP was added to the reaction solution.

The referenced  $\text{Ni}_2\text{P}$  NPs. The process for preparing  $\text{Ni}_2\text{P}$  nanoparticle is similar with the CoP seed, except 0.256 g  $\text{Ni}(\text{acac})_2$  and 4 mL TOP were used, and the final reaction temperature is  $320^\circ\text{C}$  for 2 h.

The referenced Ni NPs.  $\text{Ni}(\text{acac})_2$  (0.204 g), OAm (5 mL) and ODE (5 mL) were placed in a three-neck flask and stirred magnetically about 20 min under a flow of nitrogen (99.999%). The mixture was heated to  $120^\circ\text{C}$  and maintained for 30 min, then the temperature was raised to  $215^\circ\text{C}$  and kept for 1 h.

All the black products were obtained by centrifugation and washed with excess hexane and ethanol (Vhexane: Vethanol = 1:3). And the products were dried at  $60^\circ\text{C}$  under vacuum overnight. Note that all the reaction process including the cooling process were performed under the blanket of  $\text{N}_2$  (99.999%).

### 2.3. Characterization

X-ray diffraction (XRD, PROX-ray diffractometer with  $\text{Cu K}\alpha$  source) was used to investigate the crystalline phase. The morphology features were reflected by transmission electron microscope (TEM, Hitachi-7700 working at 100 kV), high resolution TEM (HRTEM), high-angle annular

dark-field scanning transmission electron microscope (HAADF-STEM) and the line-profile analysis (JEOL JEM-2100 F field emission electron microscope working at 200 kV), atomic resolution HAADF-STEM (Titan 80–300 scanning/transmission electron microscope operated at 200 kV, equipped with a probe spherical aberration corrector). Surface element chemical states were reflected by X-ray photoelectron spectroscopy (XPS, ULVAC PHI Quantera microscope). And all the high resolution XPS spectra were corrected by the peak of C1s. XAFS spectra were operated at 2.5 GeV with a maximum current of 250 mA at 1W1B station in BSRF (Beijing Synchrotron Radiation Facility, P. R. China). The fluorescence mode using a Lytle detector was used to obtain XAFS measurements at the Co K-edge and Ni K-edge. Graphite powder was used as a binder to pelletize the samples to disks (13 mm diameter and 1 mm thickness).

### 2.4. Electrocatalytic measurement

HER and OER tests were performed in a three-electrode system with an electrochemical workstation (CHI 760E, CH Instruments, Inc., Shanghai): a Ag/AgCl as reference electrode, a graphite rod as counter electrode and the catalyst modified Ti slice (thickness: 0.1 mm, area:  $1 \times 1 \text{ cm}^2$ ) as the work electrode. The 0.5 M  $\text{H}_2\text{SO}_4$  electrolyte and 1 M KOH electrolyte were bubbling with  $\text{N}_2$  or  $\text{O}_2$  for about 20 min to saturate, respectively. All the potentials were calibrated to reversible hydrogen electrode (RHE) and the polarization curves were iR corrected. The work electrode was prepared as follows: 10 mg of the catalyst was dispersed in 1 mL hexanes and ultrasonic at least 30 min to form a homogeneous slurry. Then 200  $\mu\text{L}$  slurry was dropped on the Ti slice with a 20  $\mu\text{L}$  increment, the final catalyst mass loading is  $2 \text{ mg} \cdot \text{cm}^{-2}$ . The decorated Ti foils were dried under ambient conditions and annealed under 5%  $\text{H}_2/\text{Ar}$  [20–22].

Linear sweep voltammetry (LSV) measurements were performed with a scan rate of  $5 \text{ mV} \cdot \text{s}^{-1}$ . Cyclic voltammetry (CV) measurements scanning at non-Faradaic potential regions with different scan rates were used to determine the double layer capacitance ( $C_{dl}$ ). Electrochemical impedance spectroscopy (EIS) experiments with frequencies ranging from  $10^5 \text{ Hz}$  to 0.1 Hz were carried out with an alternating current (AC) amplitude of 5 mV at the given potentials. The gaseous product was measured by a gas chromatography (Bruker GC450), and the Faradaic efficiencies were calculated with the reported method [23].

## 3. Results and discussion

Fig. 1a displays the synthetic process of multi-dimensional Ni/NiCoP NHs using SPT strategy. Firstly, CoP NCs (Fig. S1, Fig. S2) were synthesized through an organic solution method with  $\text{Co}(\text{acac})_2$  as metal source and trioctylphosphine (TOP) as P source in oleylamine (OAm), the resulting NCs were separated and re-dispersed in 1-octadecene (ODE). The critical step for generating multi-dimensional Ni/NiCoP NHs is the addition of the second metal precursor ( $\text{Ni}(\text{acac})_2$ ) into CoP NCs dispersion followed by heating at  $320^\circ\text{C}$  for 2 h. In this process, metallic Ni NCs formed first and then promoted further growth of NiCoP, forming strings of Ni/NiCoP core/shell structures. Powder X-ray diffraction (XRD) (Fig. S1a) confirms the two-phase existence of NiCoP and Ni. Interestingly, segregated NiCoP NCs (Fig. S1~S5) can also be prepared by adding extra TOP in the second step.  $\text{Ni}_2\text{P}$  and Ni NCs (Fig. S1, S2) were also synthesized for electrocatalytic performance comparison. A series of samples with different Ni:Co mole ratios were also synthesized, and the characterizations (Fig. S6, S7) suggested the optimal feed mole ratio for synthesizing this multi-dimensional core/shell Ni/NiCoP heterojunctions is  $\text{Co}(\text{acac})_2$ :  $\text{Ni}(\text{acac})_2 = 1:1$  (Ni/NiCoP NHs).

High-angle annular dark-field scanning transmission electron microscope (HAADF-STEM) shows that Ni/NiCoP NHs possess snap bean-like morphology (Fig. 1b). This special morphology conform to the

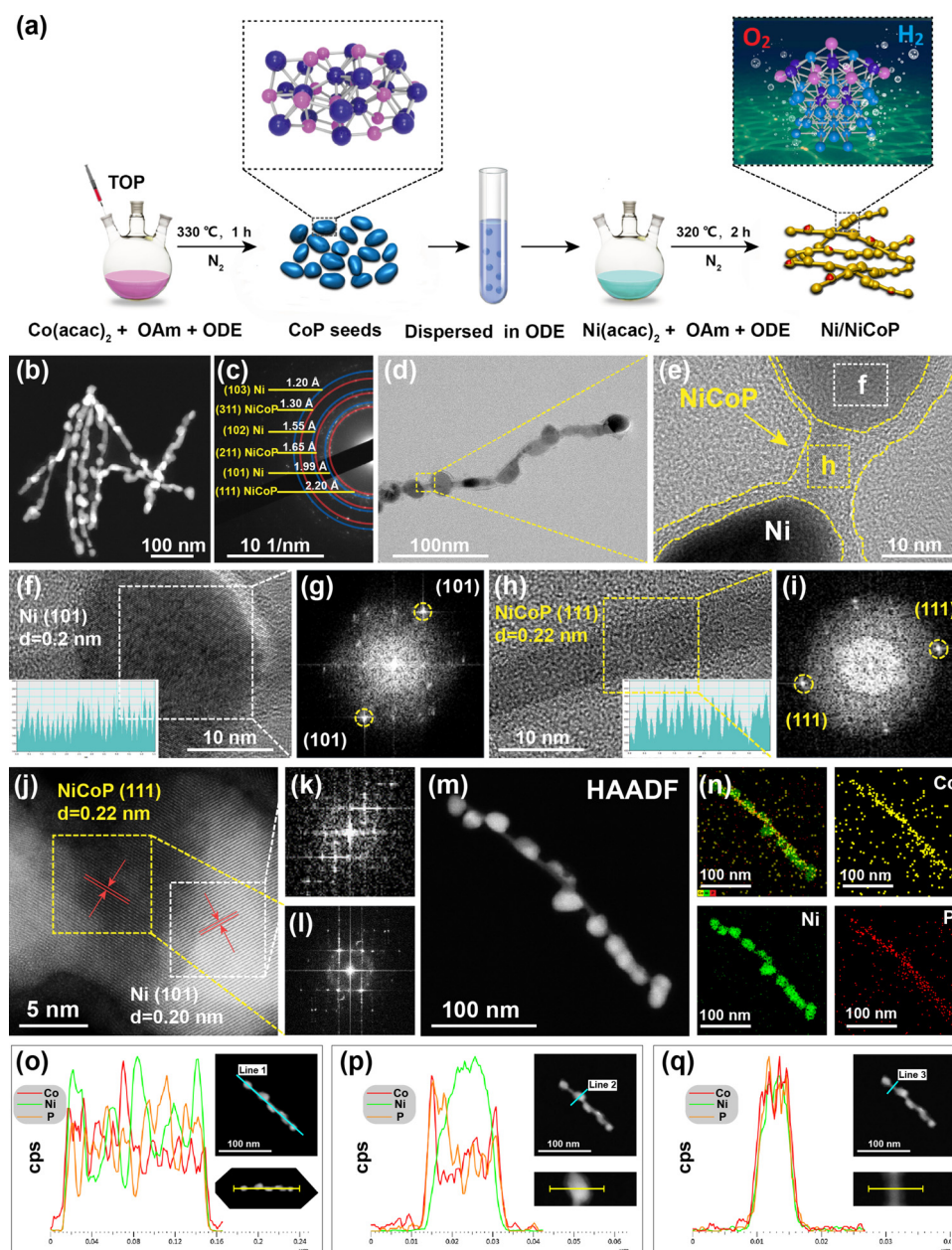


**Fig. 1.** (a) Synthesis scheme, (b) HAADF-STEM, (c) SAED, (d, e, f, h) HRTEM, (g, i) FFT of (f) and (h), (j) AC-HAADF-STEM, (k, l) FFT of (j), (m, n) HAADF-STEM-EDS mapping, (o, p, q) EDS line scanning of Ni/NiCoP NHs.

ideology of “1 + 0”, which mean the composite material is multi-dimensional with one-dimensional (1D) NiCoP nanorod and zero-dimensional (0D) Ni nanoparticles. The selected area electron diffraction (SAED) suggested that all the clear diffraction rings match well with Ni and NiCoP (Fig. 1c). High resolution TEM (HRTEM) (Fig. 1d, 1e, 1f, 1h) and spherical aberration correction (AC) (AC-HAADF-STEM) (Fig. 1j) show identifiable fringe spacing of 0.22 and 0.20 nm, which are corresponding to (111) crystal plane of NiCoP and (101) crystal plane of Ni. These crystal plane identification can be confirmed accurately by line profile (inset of Fig. 1f and 1h) and FFT images (Fig. 1g, 1i, 1k, 1l). Moreover, the energy-dispersive X-ray spectroscopy (EDS) elemental mapping images (Fig. 1m, 1n) further confirm the existence of N, Co and P elements, while Ni mainly exists in the core part of the Ni/NiCoP heterojunctions. EDS line scanning (Fig. 1o, 1p, 1q) was used to further prove the multi-dimensional core/shell Ni/NiCoP heterojunctions. Three different regions in one Ni/NiCoP heterojunctions were selected: entire heterojunctions (insert of Fig. 1o), nanoparticles part (insert of

Fig. 1p), nanochains part (insert of Fig. 1q). The corresponding EDS elements line scanning curves confirm Ni mainly exists in the core part of the nanoparticles, while the outer of the nanoparticles and the nanochain parts are consist of Ni, Co, P with a uniform distribution. All the above analyses prove Ni nanoparticles are enclosed and strung by NiCoP, forming multi-dimensional core/shell Ni/NiCoP nano-heterojunctions.

XPS was measured to reflect surface element chemical states. Obvious peaks of Ni, Co and P elements could be observed in the survey of samples (Fig. S8). Six distinct peaks belong to Ni-P (Ni 2p<sub>3/2</sub> 852.7 and Ni 2p<sub>1/2</sub> 870.1 eV), oxidized Ni species (855.7 and 873.5 eV) and satellites (861.5 and 879.4 eV) could be divided in Ni 2p spectra of Ni/NiCoP NHs, NiCoP NCs and Ni<sub>2</sub>P NCs (Fig. 2a). Similarly, Co-P (Co 2p<sub>3/2</sub> 778.1 and Co 2p<sub>1/2</sub> 793.3 eV), oxidized Co species (781.4 and 797.1 eV) and satellites (785.5 and 802.5 eV) also can be assigned in Co 2p spectra of Ni/NiCoP NHs (Fig. 2b). In P 2p region (Fig. 2c), the peak around 129.6 eV belongs to P bonds to Ni and Co, and the peak at



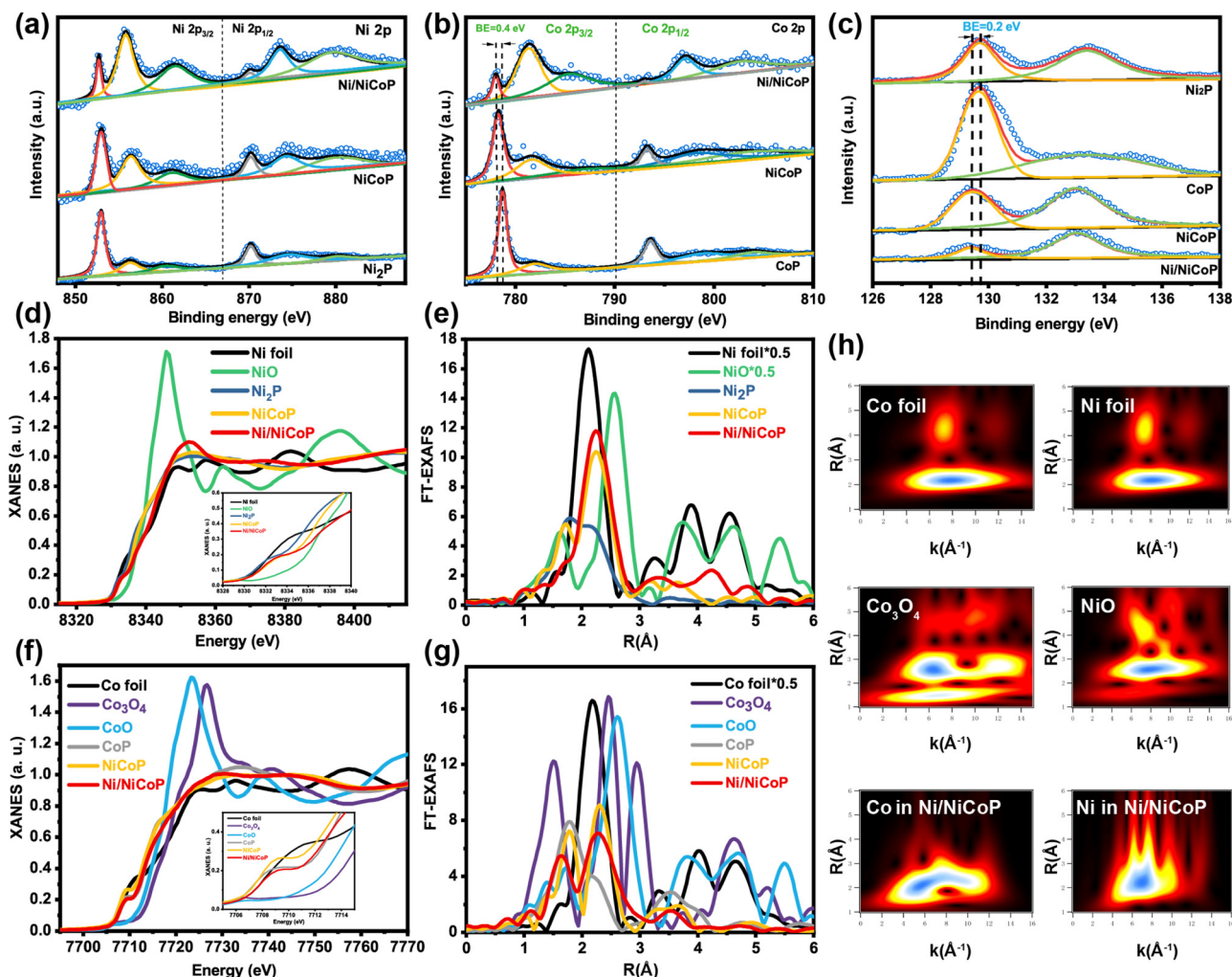


**Fig. 2.** (a–c) XPS of Ni 2p, Co 2p and P 2p spectra. (d) XANES spectra at the Ni K-edge and (e) FT at the R space of Ni foil, NiO, Ni<sub>2</sub>P, NiCoP and Ni/NiCoP. (f) XANES spectra at the Co K-edge and (g) FT at the R space of Co foil, Co<sub>3</sub>O<sub>4</sub>, CoO, CoP, NiCoP and Ni/NiCoP. (h) WT contour plots of Co foil, Ni foil, Co<sub>3</sub>O<sub>4</sub>, NiO, and Ni/NiCoP.

133.3 eV attributes to oxidized P species due to exposure to air. Interestingly, the binding energy in Co 2p spectra for Co-P bond in Ni/NiCoP NHs and NiCoP NCs locate at more negative positions ( $\sim 0.4$  eV) compared with that for CoP NCs, but higher than that of metal Co (778.1 eV). And the negative shift ( $\sim 0.2$  eV) also could be observed in P 2p spectra, suggesting the different electronic structures among Ni<sub>2</sub>P, CoP, NiCoP, NCs and Ni/NiCoP NHs, but both the Ni and Co show positive charges and P shows negative charge. All these charge property make its structure similar to that of hydrogenase, benefiting the electrocatalytic HER activity [24–26].

Synchrotron-radiation-based X-ray absorption near-edge structure (XANES) and extended X-ray absorption fine structure (EXAFS) were further carried out to demonstrate the electronic structure and coordination information. The Ni K-edge absorption threshold position (Fig. 2d) locates between the contrastive NiCoP, Ni<sub>2</sub>P and NiO, indicating the valence of Ni follows the order of Ni(NiO) > Ni(Ni/NiCoP) > Ni(NiCoP) > Ni(Ni<sub>2</sub>P) > Ni. These results reveal the formation of heterojunction greatly changes electronic structure of Ni(O). Similarly, Co K-edge absorption threshold position (Fig. 2f) suggests the valence of Co follows the order of Co(Co<sub>3</sub>O<sub>4</sub>) > Co(CoO) > Co(CoP) > Co(Ni/NiCoP) > Ni(NiCoP) > Co. These results confirm XPS analyses, suggesting the different electronic structures of Ni and Co in Ni/NiCoP NHs which may be more conducive to electrocatalytic reaction than NiCoP, Ni<sub>2</sub>P and CoP NCs. The coordination information of Ni (Fig. 2e) and Co (Fig. 2g) atoms can be confirmed by Fourier-

transformed (FT)  $k^3$ -weighted EXAFS spectra. Compared with R-space of Ni foil, NiO, Ni<sub>2</sub>P, Co foil, CoO, Co<sub>3</sub>O<sub>4</sub>, CoP and NiCoP, the peaks of Ni R-space at 1.7 and 2.25 Å, Co R-space at 1.6 and 2.3 Å can be observed in Ni/NiCoP NHs, which can be attributed to Ni-P, Ni-Co(Ni), Co-P and Co-Ni shells. Additionally, the intensity of Ni-Co(Ni) in Ni/NiCoP NHs is higher than that of NiCoP NCs, indicating the higher Ni coordination in Ni/NiCoP NHs. The structural parameters of Ni and Co atoms can be obtained by quantitative EXAFS fitting (Fig. S9 and Table S1). Moreover, wavelet transform (WT) contour plots (Fig. 2h) of Ni/NiCoP NHs show two intensity maximum at about 6 and 10 Å which also can be attributed to Co-P, Co-Ni, Ni-P, and Ni-Co(Ni) coordination by comparing with the WT plots of Co foil, Co<sub>3</sub>O<sub>4</sub>, Ni foil, and NiO.

We employed a three-electrode setup to assess HER and OER performances. The samples were dropped on Ti slice and annealed under 5% H<sub>2</sub>/Ar to remove surfactant before measurement and the effect of this treatment on the activity was clarified (Fig. S10, S11). The HER and OER electrocatalytic performance of the samples with different Ni:Co feed ratios were first measured (Fig. S12 ~ S15), and the electrochemical tests suggested Ni/NiCoP NHs (feed mole ratio is 1:1) was optimal for both HER and OER. Therefore, Ni/NiCoP NHs was selected as the target electrocatalyst. Polarization curves and Tafel curves in 0.5 M H<sub>2</sub>SO<sub>4</sub> (Fig. 3a, Fig. S16a) suggest except commercial 20% Pt/C, Ni/NiCoP NHs catalyst delivers a smaller overpotential (125 mV) at the current density of 10 mA cm<sup>-2</sup> and lower Tafel slope (70 mV dec<sup>-1</sup>) than that of NiCoP (145 mV, 75 mV dec<sup>-1</sup>), Ni<sub>2</sub>P (160 mV, 85 mV dec<sup>-1</sup>), Ni (250 mV)

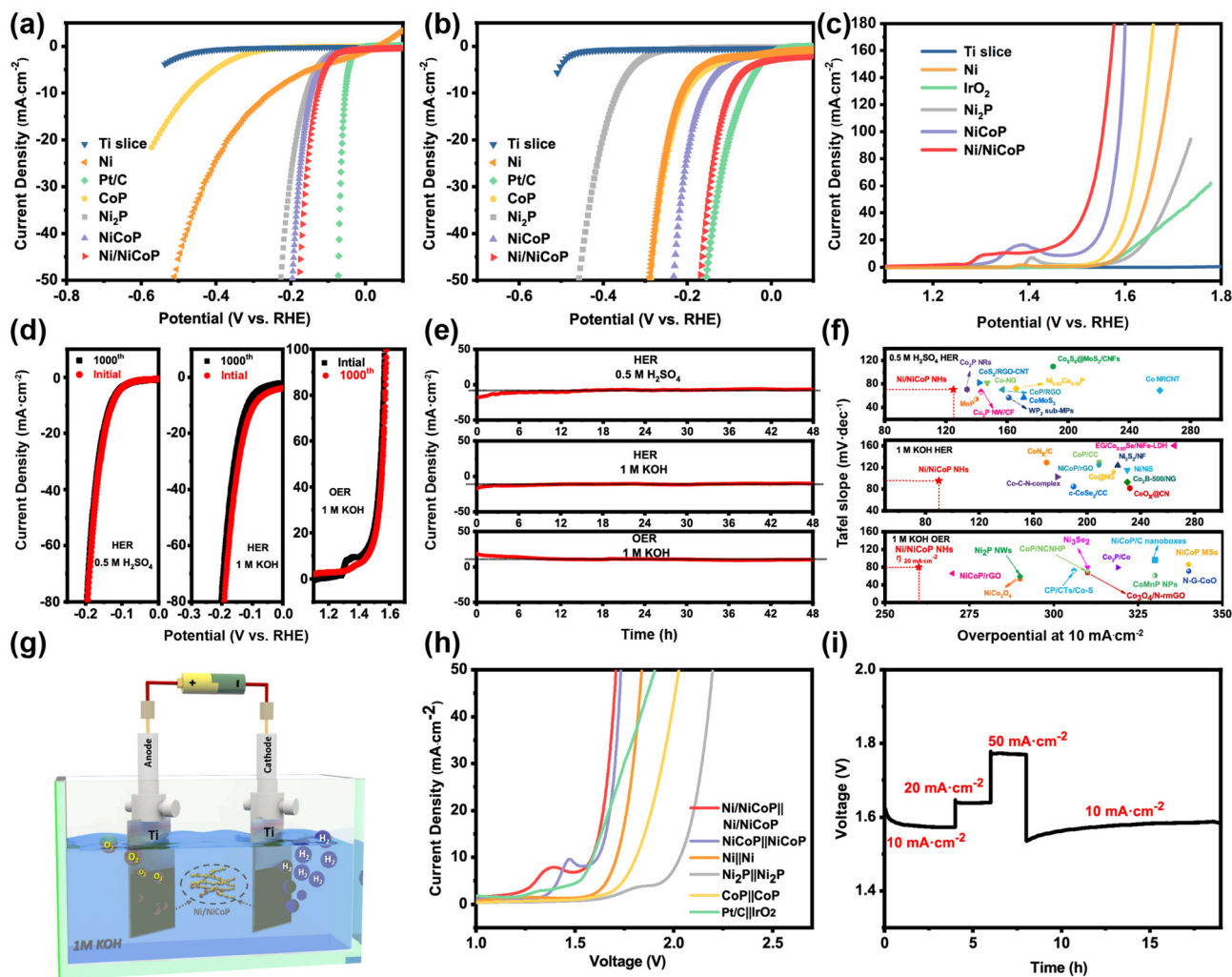


**Fig. 3.** Polarization curves of HER in (a) 0.5 M  $\text{H}_2\text{SO}_4$ , (b) 1 M KOH and (c) OER in 1 M KOH. (d) Polarization curves of Ni/NiCoP NHs before and after 1000 CV cycles. (e) Chronoamperometry curves of Ni/NiCoP NHs at the potential of 130 mV, 100 mV and 1.45 V vs. RHE for HER and OER. (f) Partial activity comparison of the overpotentials at  $10 \text{ mA}\cdot\text{cm}^{-2}$  of Ni/NiCoP NHs with reported catalysts (Table S3 ~ S5) (note: the OER overpotential at  $20 \text{ mA}\cdot\text{cm}^{-2}$  for Ni/NiCoP is compared). (g) Diagram of overall water splitting. (h) Polarization curves and (i) multi-current process using Ni/NiCoP NHs as both electrodes.

and CoP (470 mV,  $112 \text{ mV}\cdot\text{dec}^{-1}$ ), indicating the excellent HER electrocatalytic activity and kinetics [27,28]. Significantly, Ni/NiCoP NHs shows small HER overpotential of 90 and 168 mV at 10 and  $50 \text{ mA}\cdot\text{cm}^{-2}$  and low Tafel slope ( $95 \text{ mV}\cdot\text{dec}^{-1}$ ) in 1 M KOH (Fig. 3b, Fig. S16b), comparable to that of commercial Pt/C (65 and 157 mV,  $67 \text{ mV}\cdot\text{dec}^{-1}$ ), and lower than that of NiCoP (157 and 230 mV,  $99 \text{ mV}\cdot\text{dec}^{-1}$ ),  $\text{Ni}_2\text{P}$  (367 and 459 mV,  $104 \text{ mV}\cdot\text{dec}^{-1}$ ), Ni (215 and 288 mV,  $108 \text{ mV}\cdot\text{dec}^{-1}$ ) and CoP (197 and 284 mV,  $110 \text{ mV}\cdot\text{dec}^{-1}$ ). Tafel slope value of Ni/NiCoP NHs also suggest that the HER reaction follows Volmer-Heyrovsky mechanism in both acid and alkaline [29]. Electrochemical impedance spectroscopy (EIS) (Fig. S17, Table S2) suggests the smallest charge-transfer resistance ( $R_{ct}$ ) of Ni/NiCoP NHs, verifying a quick electron transfer rate [30]. Besides, Ni/NiCoP NHs also show biggest electrochemical double-layer capacitances ( $C_{dl}$ ) value (Fig. S18 ~ S19) for both HER in 0.5 M  $\text{H}_2\text{SO}_4$  and 1 M KOH, suggesting the largest electrochemical active surface area (ECSA).

The OER electrocatalytic performance was investigated in 1 M KOH. Ni/NiCoP NHs catalyst show higher current density at the same overpotential than  $\text{IrO}_2$ , NiCoP, CoP,  $\text{Ni}_2\text{P}$  and Ni (Fig. 3c). Only 260 mV vs. RHE is needed to reach the current density of  $20 \text{ mA}\cdot\text{cm}^{-2}$ . And the Tafel slope (Fig. S16c) of Ni/NiCoP NHs is  $80 \text{ mV}\cdot\text{dec}^{-1}$ , indicating the favorable reaction kinetics. Ni/NiCoP NHs catalyst was tested for 1000 cyclic voltammetry (CV) cycles in acidic/alkaline medium for HER and OER, and in neither case did the activity show a noticeable change in

polarization curves (Fig. 3d). Chronoamperometry curves (Fig. 3e) display a negligible loss at the initial time ( $\leq 5 \text{ h}$ ) due to the slight drop of active Ni/NiCoP, then the current densities keep unchanged for at least 43 h. The HER and OER electrocatalytic activity of Ni/NiCoP NHs shows significantly improvement compared to some reported highly active electrocatalysts (Fig. 3f, Table S3-S5).

TEM images of Ni/NiCoP NHs after CV cycled stability tests on HER and OER (Fig. S20) suggested the post-test Ni/NiCoP NHs almost retained the initial morphology. EDS elemental mapping images of Ni/NiCoP NHs after HER stability tests in both acid (Fig. S21) and alkaline (Fig. S22) confirmed the co-existence of Ni, Co, P. Moreover, the corresponding EDS spectra suggested Ni remained to be the main component, demonstrating the outer NiCoP indeed protected Ni cores from corrosion even in acid. High resolution Ni 2p, Co 2p and P 2p spectra (Fig. S23) suggested the chemical states of the post-HER catalyst in both acid and alkaline did not change, but the chemical states of the post-OER catalyst showed an obvious difference, signals belonged to phosphides disappeared, only broad peaks corresponding to the oxidized Ni, Co species were observed for the post-OER sample, and P element was in the similar situation, relating with the surface oxidation during the OER process. EDS line scanning of Ni/NiCoP NHs after stability tests for OER (Fig. S24) was carried to further study the element distribution, and the results showed that the outer part of the heterojunctions was oxygen richer than the inner part, conforming the surface oxidation

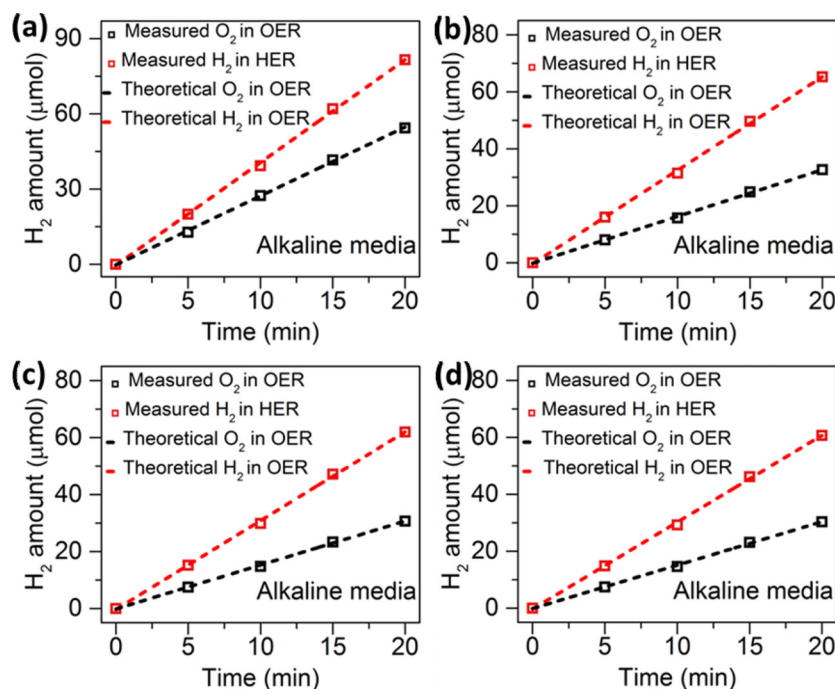


Fig. 4. Faradic efficiency of HER and OER in half-reaction at the current density of 100 mA·cm<sup>-2</sup> (a) and overall water splitting in 1 M KOH at the current density of 50 mA·cm<sup>-2</sup> (b); Faradic efficiency of overall water splitting at a current density of 50 mA·cm<sup>-2</sup> after 1 h reaction (c) and after 48 h reaction (d).

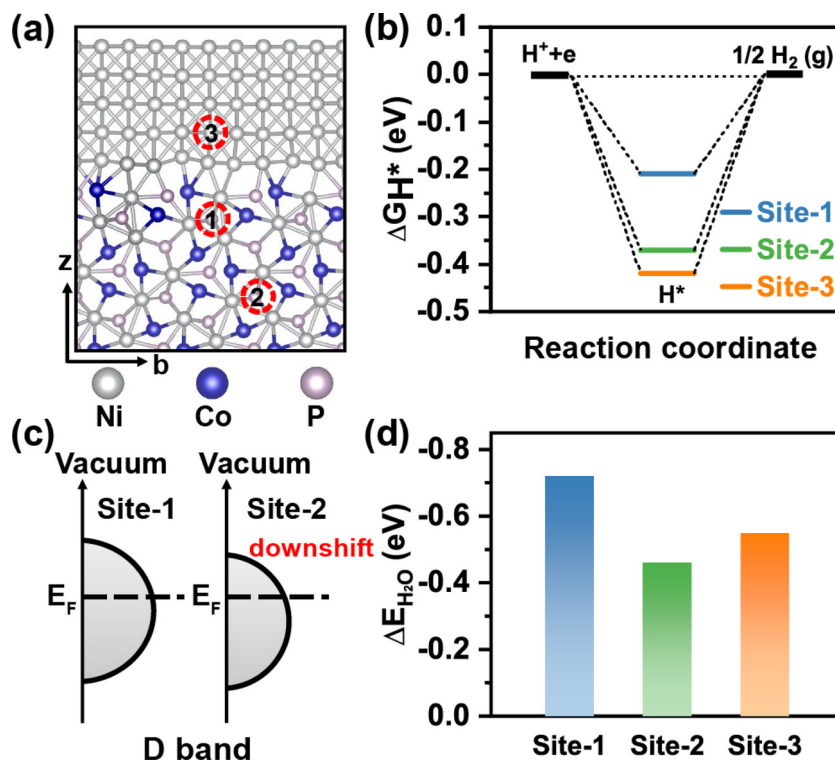


Fig. 5. (a) Schematic representation and (b) calculated  $\Delta G_{H^*}$  at three interface sites of Ni/NiCoP, (c) schematic illustration of the effect of site-1 and site-2 on the electronic structure, (d) comparison of H<sub>2</sub>O adsorption energy on site-1, site-2 and site-3.

during the OER process, and surface oxides (or hydroxides) were active species for OER as reported by previous studies [31].

Based on the above analyses, the Ni/NiCoP NHs catalyst was regarded as an efficient HER and OER (pre)electrocatalyst in alkaline solution. Therefore, we expect Ni/NiCoP NHs electrodes can act as an excellent bifunctional catalyst for water splitting in alkaline [29] (Fig. 3g). Polarization curve (Fig. 3h) of two electrode (Ni/NiCoP || Ni/NiCoP)

suggested that cell voltage of Ni/NiCoP couple at 10 mA·cm<sup>-2</sup> was 1.57 V, lower than that of NiCoP || NiCoP (1.61 V), Ni || Ni (1.71 V), Ni<sub>2</sub>P || Ni<sub>2</sub>P (2.03 V), CoP || CoP (1.81 V) and Pt/C || IrO<sub>2</sub> (1.58 V). To reach the current density of 50 mA·cm<sup>-2</sup>, only 1.71 V was needed, which is better than or parallel to most previously reported highly active bi-functional electrocatalysts (Table S6). Durability test with multi-current density (Fig. 3i) demonstrated the activity could be maintained at least



of 19 h.

The amount of gaseous products from theoretically calculation and experimentally measurement for HER and OER in half-reactions using Ni/NiCoP NHs in alkaline are shown in Fig. 4a, and the data of overall water splitting using Ni/NiCoP NHs as both anode and cathode are shown in Fig. 4b. From which we can see the theoretically calculated gas amount matches well with the experimentally measured values, suggesting that the all of the Faradic efficiencies are nearly 100%. We also tested the Faradic efficiencies in the early stage (after 1 h) and latter stages (after 48 h) of overall water splitting using Ni/NiCoP NHs as both anode and cathode as shown in Fig. 4c and Fig. 4d, the results suggest the Faradic efficiencies are nearly 100% after both 1 h and 48 h reaction, proving the excellent stability of our materials for overall water splitting.

DFT calculations of H\* adsorption free energies ( $\Delta G_{H^*}$ , \* denotes an adsorption site) and density of states (DOS) were carried out to further understand the excellent electrocatalytic performance of Ni/NiCoP NHs. An ideal  $|\Delta G_{H^*}|$  is close to zero which indicated moderate H adsorption strength, further suggesting the compromised reaction barriers of the adsorption and desorption steps in hydrogen production process [32,33]. Bimetallic NiCoP ( $\Delta G_{H^*} = -0.42$  eV) shows more favorable H\* adsorption strength than that of Ni<sub>2</sub>P ( $\Delta G_{H^*} = -0.51$  eV) (Fig. S25a). Moreover, the obviously increased charge density of DOS around Fermi level for NiCoP suggests more charge carriers are provided (Fig. S25b). For Ni/NiCoP NHs,  $\Delta G_{H^*}$  values at three interface sites were calculated (Fig. 5a, the corresponding optimized model representations for hydrogen adsorption are shown in Fig. S26), and the results show that bridge Ni site far from the surface has a more negative  $\Delta G_{H^*}$  (Fig. 5b). The negative  $\Delta G_{H^*}$  reveals the rate limiting step for HER process on NiCoP is the strong binding of H adatom, but the binding strength decreases as the distance between the HER site and the Ni/NiCoP interface decreases. To understand how interface emerging changes the electronic structure of NiCoP, DOS was also calculated (Fig. S27). According to the *d*-band theory [34], the strong binding strength of H adatom decreases as the *d*-band center of the surface downshifted from the Fermi level (Fig. 5c). In alkaline, water dissociation (Volmer step,  $H_2O + e^- = H_{ads} + OH^-$ ) is usually the rate-determining step due to the high barrier. Thus the adsorption energy of H<sub>2</sub>O molecule was further calculated. DFT calculation suggests the adsorption energy of H<sub>2</sub>O on Ni/NiCoP interface (-0.72 eV) is much more favorable than that nearby Ni or NiCoP (Fig. 5d), demonstrating the formation of Ni/NiCoP hetero-interface accelerates alkaline HER by optimizing the Volmer step.

For alkaline OER, the transition metal phosphides actually act as pre-catalyst, because the surficial oxidation occurs under the actual OER potential and is responsible for OER, so the surficial oxidation process can be calculated by DFT to reflect the OER activity. In alkaline, the hydroxyls firstly react with the substrate to form OH\*. The adsorption energy of OH\* is calculated to be -3.39 eV, indicating the hydroxyl can be strongly captured by the interface sites. The charge density difference plot further indicates the interface sites can donate electron to OH\* for generating high valence Ni/Co species (Fig. S28), which may be the real active sites for OER [35–37].

#### 4. Conclusions

In summary, a novel multi-dimensional core/shell Ni/NiCoP NHs catalyst was synthesized successfully by adopting a SPT strategy. Structural analyses showed that Ni/NiCoP NHs were composed of metallic Ni nanoparticles enclosed and strung by NiCoP. Comparative studies revealed Ni/NiCoP NHs displayed superior electrocatalytic activity than single-phased NiCoP NCs, single metallic phosphides (Ni<sub>2</sub>P and CoP) and Ni NPs for both HER and OER. XPS and XAS proved the more favorable electronic structure for electrocatalytic performance of Ni/NiCoP NHs. DFT calculations suggested more optimal binding strength of H adatom, favorable H<sub>2</sub>O adsorption energy for HER, and

strong capture of hydroxyl, high valence Ni/Co species for OER at Ni/NiCoP interface. Our study broadens the synthetic methodology of TMPs nanocatalysts with particular nano-interfaces, and Ni/NiCoP NHs electrocatalyst is promising for future water-splitting applications.

#### Declaration of Competing Interest

The authors declare that they have no known competing financial interests or personal relationships that could have appeared to influence the work reported in this paper.

#### Acknowledgements

Y. P. acknowledges the Fundamental Research Funds for the Central Universities (Grants No. 19CX02008A), China Postdoctoral Science Foundation (2017M610076, 2018T110089) and Beijing Natural Science Foundation (2184104). Y. L acknowledges the China Postdoctoral Science Foundation (2018M642726). S. L acknowledges the financial support from the National Natural Science Foundation of China (21701002). J. Z. gratefully acknowledges the financial support from the National Natural Science Foundation of China (21471160) and Taishan Scholars Program of Shandong Province.

#### Appendix A. Supplementary data

Supplementary material related to this article can be found, in the online version, at doi:<https://doi.org/10.1016/j.apcatb.2019.118039>.

#### References

- [1] S. Dutta, A. Indra, Y. Feng, H. Han, T. Song, Appl. Catal. B: Environ. 241 (2019) 521–527.
- [2] Y. Wang, B. Kong, D. Zhao, H. Wang, C. Selomulya, Nano Today 15 (2017) 26–55.
- [3] J. Wang, F. Xu, H. Jin, Y. Chen, Y. Wang, Adv. Mater. 29 (2017) 1605838.
- [4] J. Yang, H. Shin, J. Mater. Chem. A 2 (2014) 5979–5985.
- [5] Y. Huang, X. Song, J. Deng, C. Zha, W. Huang, Y. Wu, Y. Li, Appl. Catal. B: Environ. 245 (2019) 656–661.
- [6] Z. Gong, G. Wang, L. Yang, H. Liu, J. Qu, J. Li, J. Am. Chem. Soc. 138 (2016) 14686–14693.
- [7] Z. Lai, A. Chaturvedi, Y. Wang, T.H. Tran, X. Liu, C. Tan, Z. Luo, B. Chen, Y. Huang, G.H. Nam, Z. Zhang, Y. Chen, Z. Hu, B. Li, S. Xi, Q. Zhang, Y. Zong, L. Gu, C. Kloc, Y. Du, H. Zhang, J. Am. Chem. Soc. 140 (2018) 8563–8568.
- [8] J. Greeley, T.F. Jaramillo, J. Bonde, I.B. Chorkendorff, J.K. Nørskov, Nat. Mater. 5 (2006) 909–913.
- [9] M. Gong, W. Zhou, M.C. Tsai, J. Zhou, M. Guan, M.C. Lin, B. Zhang, Y.F. Hu, D.Y. Wang, J. Yang, S.J. Pennycook, B.J. Hwang, H.J. Dai, Nat. Comm. 5 (2014) 4695–4700.
- [10] Q. Ma, C. Hu, K. Liu, S.F. Hung, D. Ou, H.M. Chen, G. Fu, N.F. Zheng, Nano Energy 41 (2017) 148–153.
- [11] F. Hu, S. Zhu, S. Chen, Y. Li, L. Ma, T. Wu, Y. Zhang, C. Wang, C. Liu, X. Yang, Adv. Mater. 29 (2017) 1606570.
- [12] S. Cao, Y. Chen, C.J. Wang, X.J. Lv, W.F. Fu, Chem. Comm. 51 (2015) 8708–8711.
- [13] P. He, X.Y. Yu, X.W. Lou, Angew. Chem. Int. Ed. 56 (2017) 3897–3900.
- [14] C. Tan, J. Chen, X.J. Wu, H. Zhang, Nat. Rev. Mater. 3 (2018) 17089.
- [15] H. Liang, A.N. Gandhi, D.H. Anjum, X. Wang, U. Schwingenschlogl, H.N. Alshareef, Nano Lett. 16 (2016) 7718–7725.
- [16] C. Zhu, A.L. Wang, W. Xiao, D. Chao, X. Zhang, N.H. Tiej, S. Chen, J.N. Kang, X. Wang, J. Ding, J. Wang, H. Zhang, H.J. Fan, Adv. Mater. 30 (2018) e1705516.
- [17] Y. Kim, J.W. Hong, Y.W. Lee, M. Kim, D. Kim, W.S. Yun, S.W. Han, Angew. Chem. Int. Ed. 56 (2017) 3897–3900.
- [18] J. Zhang, T. Wang, D. Pohl, B. Rellinghaus, R. Dong, S.H. Liu, X.D. Zhuang, X.L. Feng, Angew. Chem. Int. Ed. 55 (2016) 6702–6707.
- [19] Q. Xu, H. Jiang, H. Zhang, Y. Hu, C. Li, Appl. Catal. B: Environ. 242 (2019) 60–66.
- [20] E.J. Popczun, C.G. Read, C.W. Roske, N.S. Lewis, R.E. Schaak, Angew. Chem. Int. Ed. 53 (2014) 5427–5430.
- [21] Z. Huang, Z. Chen, Z. Chen, C. Lv, M.G. Humphrey, C. Zhang, Nano Energy 9 (2014) 373–382.
- [22] D.H. Ha, B. Ha n, M. Risch, L. Giordano, K.P.C. Yao, P. Karayaylali, S.H. Yang, Nano Energy 29 (2016) 37–45.
- [23] Y. Lyu, R. Wang, L. Tao, Y. Zou, H. Zhou, T. Liu, Y. Zhou, J. Huo, S.P. Jiang, J. Zheng, S. Wang, Appl. Catal. B: Environ. 248 (2019) 277–285.
- [24] Z. Xing, Q. Liu, A.M. Asiri, X. Sun, Adv. Mater. 26 (2014) 5702–5707.
- [25] P. Jiang, Q. Liu, Y. Liang, J. Tian, A.M. Asiri, X. Sun, Angew. Chem. Int. Ed. 53 (2014) 12855–12859.
- [26] Z. Li, M. Shao, L. Zhou, R. Zhang, C. Zhang, J. Han, M. Wei, D.G. Evans, X. Duan, Nano Energy 20 (2016) 294–304.

- [27] Q. Yan, H. Fan, H. Yu, Y. Zhang, Y. Zheng, Z. Dai, Y. Luo, B. Li, Y. Zong, *Angew. Chem. Int. Ed.* 56 (2017) 12566.
- [28] Y. Shi, B. Zhang, *Chem. Soc. Rev.* 45 (2016) 1529–1541.
- [29] J. Tian, Q. Liu, A.M. Asiri, X. Sun, *J. Am. Chem. Soc.* 136 (2014) 7587–7590.
- [30] D. Wang, Q. Li, C. Han, Z. Xing, X. Yang, *Appl. Catal. B: Environ.* 249 (2019) 91–97.
- [31] G. Zhang, G. Wang, Y. Liu, H. Liu, J. Qu, J. Li, *J. Am. Chem. Soc.* 138 (2016) 14686–14693.
- [32] E. Skúlason, V. Tripkovic, M.E. Björketun, S. Gudmundsdóttir, G. Karlberg, J. Rossmeisl, T. Bligaard, H. Jónsson, J.K. Nørskov, *J. Phys. Chem. C* 114 (2010) 18182–18197.
- [33] B. Hinnemann, P.G. Moses, J. Bonde, K.P. Joergensen, J.H. Nielsen, S. Horch, I. Chorkendorff, J.K. Nørskov, *Cheminform* 36 (2005) 5308–5309.
- [34] J.J. Collins, C.C. Chow, T.T. Imhoff, *Nature* 376 (1995) 236–238.
- [35] K. Wan, J. Luo, C. Zhou, T. Zhang, J. Arbiol, X. Lu, B. Mao, X. Zhang, J. Fransaer, *Adv. Funct. Mater.* 29 (2019) 1900315.
- [36] B. Zhang, X. Zheng, O. Voznyy, R. Comin, M. Bajdich, M. Garcia-Melchor, L. Han, J. Xu, M. Liu, L. Zheng, F.P. Garcia de Arquer, C.T. Dinh, F. Fan, M. Yuan, E. Yassitepe, N. Chen, T. Regier, P. Liu, Y. Li, P. De Luna, A. Janmohamed, H.L. Xin, H. Yang, A. Vojvodic, E.H. Sargent, *Science* 352 (2016) 333–337.
- [37] D. Friebe, M.W. Louie, M. Bajdich, K.E. Sanwald, Y. Cai, A.M. Wise, M.J. Cheng, D. Sokaras, T.C. Weng, R. Alonso-Mori, R.C. Davis, J.R. Bargar, J.K. Nørskov, A. Nilsson, A.T. Bell, *J. Am. Chem. Soc.* 137 (2015) 1305–1313.